

# High-efficiency Wavelength Tunable Monolayer LED with Hybrid Continuous-pulsed Injection

**Yi Zhu**

Australian National University <https://orcid.org/0000-0003-2059-3870>

**Bowen Wang**

Australian National University

**Ziyuan Li**

The Australian National University <https://orcid.org/0000-0001-9400-6902>

**Jian Zhang**

The Australian National University

**Yilin Tang**

The Australian National University

**Juan F Torres**

The Australian National University <https://orcid.org/0000-0002-3054-8638>

**Wojciech Lipiński**

The Australian National University <https://orcid.org/0000-0001-5478-6887>

**Lan Fu**

Australian National University

**Yuerui Lu** (✉ [yuerui.lu@anu.edu.au](mailto:yuerui.lu@anu.edu.au))

Research School of Engineering, College of Engineering and Computer Science, The Australian National University, Canberra, ACT, 2601 <https://orcid.org/0000-0001-6131-3906>

---

## Article

**Keywords:** High-efficiency and wavelength-tunable light emitting diode (LED), WS2 monolayer LED, electroluminescence (EL) emission

**Posted Date:** November 30th, 2020

**DOI:** <https://doi.org/10.21203/rs.3.rs-110731/v1>

**License:**  This work is licensed under a Creative Commons Attribution 4.0 International License.

[Read Full License](#)

---

# Abstract

High-efficiency and wavelength-tunable light emitting diode (LED) devices will play an important role in future advanced optoelectronic systems. Traditional semiconductor LED devices typically have a fixed emission wavelength that is determined by the energy of the emission states. Here, we developed a novel high-efficiency and wavelength-tunable monolayer WS<sub>2</sub> LED device, which operates in the hybrid mode of continuous-pulsed injection. This hybrid injection enables highly enhanced emission efficiency (> 20 times) and the effective size of emission area (> 5 times) at room temperature. The emission wavelength of WS<sub>2</sub> monolayer LED device can be tuned over more than 40 nm by driving AC voltages, from exciton emission to trion emission, and further to defect emissions. The quantum efficiency of defect electroluminescence (EL) emission is measured to be more than 24.5 times larger than that from free exciton and trion EL emissions. The separate carrier injection in our LED also demonstrate advantage in allowing to visualize and distinguish defect species in real space. Those defects are assigned to be negatively charged defects. Our results open a new route to develop high-performance and wavelength-tunable LED devices for future advanced optoelectronic applications.

## Introduction

Layered transition metal dichalcogenide (TMD) monolayers have attracted considerable interest for their unique electronic and optical properties.<sup>1-6</sup> These monolayers exhibit direct bandgap nature with high quantum yield of light emission and are of particular interest for novel optoelectronic device applications, such as a light emitting diode (LED).<sup>7,8</sup> Monolayer LED was demonstrated by forming a horizontal p-n junction using electrostatic gates.<sup>8</sup> LEDs based on vertically stacked heterostructures with hexagonal boron nitride tunnel barriers have also been reported.<sup>7,9</sup> These two types of LED devices are based on direct current (DC) injection configuration and require complicated device structures. As the counterpart of the DC driving LED, the alternating current (AC) driving LED, also known as pulsed LED, has attracted more attention recently.<sup>10,11</sup> Compared with DC LED structure, the AC LED only uses two-terminal capacitor structure *via* a single metal semiconductor contact, which significantly simplifies the fabrication. The electron charging and discharging effect in this capacitor structure will lead to pulsed light emission. In a DC LED device, electrons and holes are injected simultaneously,<sup>7</sup> while in a AC LED, electrons or holes are injected separately under different AC voltage polarities.<sup>10</sup> This separate injection feature opens a promising way to fabricated pulsed LED devices,<sup>12</sup> and allows us to probe electroluminescence (EL) emission pathway and the carrier dynamic down to each injection cycle.<sup>13</sup> However, the recombination of electrons and holes can only occur on the contact edge between electrodes and 2D monolayer material, thus EL emission effective area is small. This drawback requires a very dense electrode pattern for large-size LED devices, resulting in a bottleneck for the emerging AC-driving LED technology. In this work, we developed a novel hybrid continuous-pulsed injection method in an AC-driving LED device, which enables electron-hole recombination to occur in areas far away from the metal-semiconductor contract edge. This can highly increase the effective EL emission area, enabling a

more facile fabrication of electrode patterns and thus contributing to the adoption of pulsed LED technology.

On the other hand, wavelength-tunable LED devices are important and can enable many advanced optoelectronic applications.<sup>8, 14, 15</sup> However, most semiconductor LED devices demonstrated so far have a fixed emission wavelength, which is determined by the energy of the emission states, such as band gap edge,<sup>16, 17</sup> excitons,<sup>7, 18, 19</sup> or defects.<sup>20</sup> Here, we demonstrated a wavelength tunable AC-driving WS<sub>2</sub> monolayer LED device. Its EL wavelength can be switched from exciton to trion emission, and finally to the defect emissions, by controlling the frequency of the driving signal. Thanks to the unique feature of separate injection of electrons and holes in the AC-driving LED platform, it allows us to visualize and distinguish defect species and the evolution of defect states. The quantum efficiency of the defect EL emission was measured to be ~24.5 times larger than free exciton and trion EL emissions. Our results provide crucial insights into optimizing the performance of AC-driving LED devices for future practical applications and open a new route to study the defect states and defect engineering for the tunable LED device.

## Results

### High-efficiency monolayer LED with hybrid continuous-pulsed injection.

For LED device fabrication (Fig. 1a inset and Fig. S1), a mechanically exfoliated monolayer WS<sub>2</sub> flake was drily transferred onto a SiO<sub>2</sub>/Si substrate (275 nm thermal oxide on n<sup>+</sup>-doped silicon), in contact with a gold electrode that was peel-transferred onto monolayer sample<sup>21, 22</sup>. Part of the 1L WS<sub>2</sub> was under the gold electrode and the other part on the SiO<sub>2</sub> substrate. The measured EL emission spectrum, under AC voltage driving, was comparable with the photoluminescence (PL) spectrum from monolayer WS<sub>2</sub> (Fig. 1a). A large effective area of EL light emission (Fig. 1b) was observed from this monolayer WS<sub>2</sub> LED device (Fig. 1b inset). Figure 1c shows the emission profile along the solid white line in Fig. 1b. We observed EL emissions from locations that are 25 μm away from the edge of metal contact, which is around 5 times larger than the maximum length (~ 5 μm) reported before<sup>10</sup>. The driving voltage and frequency dependent EL emission were also measured (Figs. S2 and S3).

In order to understand this ultra-long EL emission length, time resolved electroluminescence (TREL) measurements were performed (Fig. 1d). Two EL decay curves (Fig. 1d) from the WS<sub>2</sub> LED device emerged at both voltage rising and falling edges, showing dramatically different shapes, and indicating the different carrier recombination mechanisms in these two decay processes. The hybrid continuous-pulsed EL emission observed in 1L WS<sub>2</sub> LED device (Fig. 1d) is in sharp contrast to the symmetry pulsed EL decay curves observed from 1L WSe<sub>2</sub> LED devices from both previous report<sup>10</sup> and our control experiments (Fig. S4). The entire EL decay curve from 1L WS<sub>2</sub> was divided into four phases labeled as I, II, III and IV (Fig. 1d). The corresponding schematic band diagrams were illustrated in Fig. 1e. In phase I, when the driving voltage was quickly switched from - 6.6 V to + 6.6 V, the energy band was bent

upwards, leading a large number of holes injected into WS<sub>2</sub> samples within a short period of time. The injected holes recombined with remaining electrons from previous cycle that did not have time to escape, resulting in a fast EL emission (low intensity shoulder in Fig.1d). Those remaining electrons (labeled by purple color in Fig. 1e panel I) were of different origin from those electrons due to the initial naturally n-type doping (labeled with red color). In phase II, the driving voltage was stabilized at + 6.6 V, the holes were continuously injected into 1L WS<sub>2</sub>. Due to the naturally n-type doping in 1L WS<sub>2</sub>, the injected holes could find excess electrons to form excitons and emitted light as illustrated in Fig. 1e panel II. The population of injected holes was far less than that of those free electrons from initial n-doping. The free electrons could move towards the Au metal edge and recombined with the holes continuously injected into 1L WS<sub>2</sub>, leading to a steady increase of the EL intensity with time. In phase III, the injected holes would diffuse inward accompanying with radiative recombination until they reached their longest diffusion length. Therefore, the emission area was extending inward from Au contact edge towards the far end and finally it generated an ultra-long emission length as depicted in Fig. 1e panel III. In the meantime, the EL intensity reached its maximum and then slowly decays with time. During this process, the Au contact continuously injected holes into the system to compensate holes consumption. This caused an almost flat decay curve and an ultra-long decay lifetime. Here, the EL decay curve also explained the long EL emission time. Thus, this EL decay lifetime can be approximated to EL emission time. Actually, the EL emission time can be further extended if the AC frequency is decreased (Supplementary Fig. S5). The longest EL emission lifetime in our WS<sub>2</sub> AC LED device was found to be ~1980 ns when AC frequency was 200 kHz. This ultra-long EL lifetime was attributed to the high quality WS<sub>2</sub> sample and contamination-free device fabrication method (Supplementary Note 1). In phase IV, when the applied AC voltage suddenly change its polarity (from +6.6 V to - 6.6V), the negative bias voltage quickly bent the energy band downwards, leading to the injection of a large number of electrons into 1L WS<sub>2</sub>. The injected electrons recombined with remaining holes from previous cycle that did not have time to escape (labeled by cyan color in Fig.1e panel IV), resulting in a short and intensive emission pulse (Fig.1d and Fig.1e panel IV). After the depletion of free holes, no more light emission was detected even when a negative voltage bias was still applied. In phase IV, the light emission area was very close to Au contact edge because electrons and holes only meet in the region close to the metal edge.

Here, we defined phases I and IV as pulsed injection/emission processes, while phases II and III as continuous injection/emission processes. The integrated EL intensities for both continuous mode (phases II and III) and pulsed mode (phases I and IV) were extracted as a function of AC frequency (Fig. S6a). The total contribution of EL intensity from pulsed emissions did not change when the frequency increased. However, the EL intensity from continuous emissions dramatically increased with frequency increased. The intensity ratio between continuous emissions and pulsed emissions was much larger than 1 and it reached a maximum value of ~24 under a driving frequency of 1 MHz (Fig. S6b). These results suggest that the continuous injection mode plays a significant role in improving the overall efficiency of 1L WS<sub>2</sub> AC LED devices.

The n-type 1L WS<sub>2</sub> LED device operates in a hybrid continuous-pulsed mode (with four phases I–IV), which is in sharp contrast to the purely pulsed mode (with only phases I and IV) observed in 1L WSe<sub>2</sub> LED device with neutral initial doping<sup>10</sup>. 1L WSe<sub>2</sub> sample shows neutral initial doping<sup>23-25</sup>, while the monolayer WS<sub>2</sub> sample shows naturally n-type doping because of its natural sulfur vacancy<sup>26</sup>. The n-type doping level of 1L WS<sub>2</sub> used in LED device can be estimated to be  $7.5 \times 10^{11} \text{ cm}^{-2}$  by using gate dependent PL spectra (Supplementary Note 2). In order to further confirm that the operation of the hybrid continuous-pulsed mode in 1L WS<sub>2</sub> LED device is attributed to the initial doping, we used a p-type chemical doping technique to tune the initial doping of 1L WS<sub>2</sub> sample. We found that the continuous mode can be significantly modulated using this method (Fig. S7 and Supplementary Note 4).

### Temperature dependent EL emission.

The initial doping normally comes from thermally activated free carriers and they should be very sensitive to temperature. In order to further explore and understand the dynamics of this hybrid continuous-pulsed EL emission, temperature dependent EL mappings and TREL measurements were performed. In Fig. 2a–d, we show the EL emission mapping of the monolayer WS<sub>2</sub> under four different temperatures, with fixed driving voltage ( $V_{ac} = 7.5 \text{ V}$ ) and frequency (500 kHz). A clear trend of EL quenching and emission area shrinking towards the Au electrode were observed when the temperature decreased. For comparison, the cross-section profiles of EL emission along the solid white line under 290 K and 80 K were extracted as shown in Fig. 2e and f, respectively. The EL emission length, which is defined as the distance value of full width at half maximum of EL emission profile, decreased from 5.822  $\mu\text{m}$  at room temperature to 0.016  $\mu\text{m}$  at 80 K, leading to an ultrahigh shrinking factor of 364 times in the latter scenario. The temperature dependent EL emission length was further extracted and shown in Fig. 2g. The corresponding EL emission mapping images were presented in Supplementary Fig. S8. The emission length saturated when temperature was higher than 230 K, which might result from the limited size of this specific 1L WS<sub>2</sub> sample (Fig. 2a inset). When the temperature was below 230 K, the EL emission length dramatically decreased as temperature decreased. The measured data can be perfectly fitted by the traditional temperature dependent carrier mobility model indicated in Fig. 2g red curve (Supplementary Note 5). In this AC driving LED structure, the injected carriers firstly tunneled through the air barrier under Au electrode into the monolayer WS<sub>2</sub> sample. Then, those accumulated carriers laterally diffused inward the monolayer WS<sub>2</sub>. Therefore, the emission length is highly related with carrier diffusion ability as well as mobility. Considering this emission principle, the hole diffusion length can be considered as proportional to emission length. In 1L WS<sub>2</sub>, the carrier mobility is attributed to two facts: impurity scattering and phonon scattering from crystal lattice. Normally, the mobility increases when temperature decreases,<sup>26</sup> owing to the reduction of phonon scattering. However, for doped samples, the carrier mobility decreases when temperature decreases at low temperature due to the enhanced impurity scattering from the high impurity concentration.<sup>27</sup> Phonon scattering then dominates at a higher temperature, while impurity scattering dominates at low temperature. For our monolayer WS<sub>2</sub> sample, the initial impurity

concentration was high (Supplementary Note 1). Thus, when temperature decreased, the carrier mobility decreased, leading to a short carrier diffusion length and a short emission length (Supplementary Note 5).

The EL emission intensity from the same single point (indicated in Fig. 2a) as a function of temperature is presented in Fig. 2h. The EL intensity monolithically decreased with temperature. We attribute this to the reduction of intrinsic carrier concentration which are thermally activated. The measured temperature dependent EL intensity data was well fitted by a thermal-activation model (Supplementary Note 6), as shown by the red fitting line in Fig. 2h. From the fitting, the ionization energy can be extracted to be 140.4 meV, which reasonably matches with the calculated activation energy of our Cl-doped WS<sub>2</sub> (~180 meV)<sup>28</sup>.

In order to understand the temperature dependent carrier injection dynamics in time domain, temperature dependent TREL measurements were also performed and presented in Fig. 2i. The corresponding temperature dependent PL and EL spectrum are presented in Fig. S9. At the 290 K, a hybrid continuous-pulsed injection/emission mode with four phases was observed, as previously discussed. However, the pulsed injection/emission in phases I and IV vanished when the temperature was lower than 200 K. This suggests that a completely pulsed AC LED device<sup>10</sup> might not operate at low temperature, owing to the possibility of remaining carriers escape quickly at low temperature when switching the polarity of voltage bias (Fig. 1e panels I and IV). On the other hand, the continuous mode (phases II and III) can still operate at low temperature (Fig. 2i). The EL emission intensity and lifetime from phases II and III also significantly reduce as temperature decrease from 290 to 80 K. This behavior is consistent with thermally activated free carrier model presented above. When temperature decreased, the population of thermally activated electrons and holes will both reduce. The TREL oscillation may come from the current oscillation from our instruments (Supplementary Fig. S10 and Supplementary Note 7).

### **Wavelength-tunable EL emission modulated by AC driving frequency.**

At 80 K, the EL emission peak wavelength can be tuned from 599 nm (exciton emission), to 609.6 nm (trion emission), further to 628 nm (defect state 1, D1) and 638 nm (defect state 2, D2) (Fig. 3a and Supplementary Fig. S11), when the AC driving frequency changes from 100 kHz to 1 MHz. Those two defect emission peaks from EL spectra match with the defect peaks from PL spectra (Fig. S13). Under low driving frequencies (<300 kHz), the exciton and trion emissions dominate the EL spectra (Fig. 3a top panels). When the driving frequency is higher than 300 kHz, the emission from defect state 1 (D1) start to become dominant; when the driving frequency is higher than 800 kHz, the emission from defect state 2 (D2) start to become dominant in the EL spectra (Fig. 3a,b and Supplementary Fig. S11).

This wavelength tunability by AC driving frequency can be explained by the driving frequency dependent electrical doping to the 1L WS<sub>2</sub> sample. In each cycle of AC LED operation, there are more electrons than holes injected into 1L WS<sub>2</sub>, leading to an effective n-type doping. A higher driving frequency will effectively lead to a higher n-type doping to 1L WS<sub>2</sub> samples. This is evidenced by following three folds. Firstly, the Fermi level of Au metal was pinned close to the conduction band of 1L WS<sub>2</sub>, which is suggested by the slightly unipolar transport curves measured from a 1L WS<sub>2</sub> field effect transistor (FET)

device (Supplementary Fig. S12). The close-to-conduction Fermi pinning will be more beneficial to the injection of electrons than holes. Secondly, the measured integrated PL from phases II and III per cycle increased when the driving frequency increases (Fig. S4b), which suggested that the 1L WS<sub>2</sub> gets more n-doped as driving frequency increases. Thirdly, at 80 K, the PL intensity ratio between trion and exciton peaks increased when driving frequency is switched from 100 kHz to 200 kHz.

The observed defect states (D1 and D2) might be the charged defect states sitting above the valence band maximum, which have been demonstrated by both experiments and theoretical calculations in 1L WS<sub>2</sub>.<sup>29</sup> Under low driving frequency, 1L WS<sub>2</sub> sample has a low n-type doping and the quasi Fermi level of holes is below the defect levels (Fig. 3c). The defect levels are fully occupied by holes and will be involved in the EL process. When the AC driving frequency increases, the quasi Fermi level of holes moves upward, causing the defect levels to be unoccupied. The injected holes can be quickly captured by those defect levels, resulting in the transition of the EL emissions from exciton/trion to the lower-energy defect states (Fig. 3a,b).

The ratio between the integrated EL intensities from those two defects and that from exciton is also plotted as a function of driving frequency (Fig. 3b inset). The ratio value for D1 was around 10 for frequencies greater than 600 kHz, while the ratio value for D2 (with larger trapping potential) reached a maximum of 24.5 at 900 kHz. Those values suggest highly enhanced internal quantum efficiencies from the electrically pumped defect states in 1L WS<sub>2</sub> than that from free excitons (Supplementary Note 8), which is hardly seen in optically pumped WS<sub>2</sub> monolayer samples<sup>30</sup> (Fig. S13). In an optical pumping process, electrons and holes are optically excited under certain optical selection rules and they can relax into conduction band minima and valence band maxima to forming free excitons quickly<sup>30</sup>. Those free excitons can recombine radiatively before they are captured by the defect-induced traps<sup>30</sup>. In sharp contrast to the optical excitation, the electrical pumping will inject carriers to conduction or valence bands without strict selection rules. Those randomly injected electrons or holes will take a much longer time to form excitons (Fig. 2i). Those defect states can capture electrons and holes, facilitating the formation of excitons, leading to higher quantum yield from those defect states.

To understand the origin of the large enhancement of quantum yield from the defect states, we used TREL to characterize the time resolved emission dynamics of the defects, exciton and trion species as depicted in Fig. 3d. From the TREL curves, it took 170.2 and 156.8 ns for exciton and trion emissions to reach the maximum value, respectively; in contrast, the required time to reach the two defect states, D1 and D2, are 14.3 and 15.9 ns, respectively, a much shorter time than for free excitons and trions. This confirms the above explanation that defects states can facilitate the formation of excitons in 1L WS<sub>2</sub> AC driven LED device. Likewise, the radiative EL emission lifetime for D1 and D2 were measured to be 46.6 ns and 43.3 ns, respectively, i.e. much shorter than those from free excitons (181.2 ns) and trion (192.4 ns). This further confirms the explanation that those defect states can result in enhanced EL quantum yield.

## Visualization of exciton/trion to defect emission transition and defect level evolution.

Visualizing the spatial distribution of EL emissions from individual defects would allow us to better understand their transition dynamics, and thus to design high performance lighting devices. Here we conducted the low temperature EL mapping measurements and directly visualized the transition dynamics of three individual defects in 1L WS<sub>2</sub> AC driving LED devices. Figure 4 a–c show the EL emission images in real space from the AC driving WS<sub>2</sub> LED device with different driving frequency. Three bright emission spots were observed (labelled as S1, S2 and S3) under driving frequency of 200 kHz. When the driving frequency increased, the middle spot S2 emerged and became the dominant bright spot. By converting the spatial axis, which is perpendicular to the edge of Au electrode (dashed line shown in Fig. 4a–c), to wavelength dimension, the EL spectra collected from three narrow rectangular areas (a width of 95 μm) covering those three spots, respectively, were extracted as shown in Fig. 4d–f. The extraction method is provided in the method section and Supplementary Fig. S15. Under driving frequency of 200 kHz, the EL spectra for S1 and S2 contains a significant contribution from defect states, while the contribution from exciton and trion dominated the EL spectra of S3. Under the driving frequencies of 600 kHz and 1MHz, the defect emissions dominated the EL spectra for all three areas. Interestingly, the central defect emission wavelength was found at 628 nm (D1) for S1 and 638 nm (D2) for S2 and S3. Note that the intensity from S2 was more than 10 times higher than that from S3, despite coming from the same defect state D2. This suggests that the local doping level is highly uniform and might be significantly affected by the appearance of the defects.

Here, we have successfully distinguished different defect types and visualized the evolution of different individual defects in real space by using this AC driving EL emission mapping. The origin of two defect emissions (D1 and D2) was attributed to the localization of excitons in the negatively charged defects type I,<sup>29</sup> which has been observed by scanning tunneling microscopy/spectroscopy (STM/STS) and CO-tip noncontact atomic force microscopy (nc-AFM). On basis of STS, the negatively charged defects type I exhibit electronic signatures showing several states above the valence band maximum,<sup>29</sup> which is consistent with our experimental observation.

In our experiment, the beauty of our AC injection is that it can separately injects holes or electrons. In this way, it provides a better chance for us to monitor injection dynamics. The EL defect emission in our sample only appears in hole injection section as shown in TREL measurement (Fig. 3c), which is consistent with STS  $dI/dV$  spectra results.<sup>29</sup> This suggests that the two defect states in our experiment are negatively charged. They prefer trap holes rather than electrons. On the basis of the STS  $dI/dV$  spectra, we attribute the emission peaks of 628 nm and 638 nm to the negatively charged type I defects with different energy depth. Those negatively charged defects can be triggered by increasing AC driving frequency as shown in Fig. 4g.

In summary, we demonstrated a novel hybrid continuous-pulsed injection method in an AC driving LED device, which allows electron-hole recombination to occur in the areas far away from the metal-semiconductor contract edge. This led to a large increase of the effective emission areas and emission

efficiency in an AC driving LED device. The continuous-pulsed injection concept demonstrated in this work can be extended to other 2D materials under this AC driving LED structure for achieving a larger effective emission area and reducing fabrication costs. Moreover, the wavelength-tunable AC driving WS<sub>2</sub> monolayer LED device was demonstrated. Its EL emission wavelength can be switched from exciton to trion emission, and finally to the defect emissions, by controlling the frequency of the driving signal. The quantum efficiency of defect EL emission was measured to be ~24.5 times larger than free exciton and trion EL emission. The ability to realize high intensity defect emission opens opportunities in the field of defect engineering and defect based single photon emission. In addition, thanks to the unique feature of separate injection of electrons and holes in the AC driving LED platform, we could visualize and distinguish defect species and the evolution of defect states in real space. Those defect levels were assigned to negatively charged defects. Our results not only illustrate important insights for further understanding the AC LED working principle and providing a general guideline for rationally designing high performance AC driving LED, but they also open a new route to study the defect states and defect engineering for the tunable LED device.

## Methods

**Device fabrication.** The monolayer WS<sub>2</sub> and WSe<sub>2</sub> samples were mechanically exfoliated onto the SiO<sub>2</sub>/Si substrate where had been already patterned 100 nm thickness gold electrodes by conventional photolithography. Another 100 nm thickness gold electrode was peeled off from SiO<sub>2</sub>/Si substrate through a homemade micromanipulator and then drop it between samples and electrodes to bridge them together. The WS<sub>2</sub> crystal was purchased from HQ graphene with chemical vapor transport (CVT) growth method containing Chlorine (Cl). The WSe<sub>2</sub> crystal was purchased from 2D semiconductor with flux zone growth method containing no halide elements.

### Optical characterization.

PL and EL measurements were conducted using an in-house developed photoluminescence setup equipped with an Andors iDu416 charge-coupled detector and a Kymera 328i spectrometer. A 532 nm diode-pumped solid state (DPSS) laser was used as the excitation source. The EL signal was generated by applying an amplified square wave generated from the function generator. All EL related measurements were conducted with a microscope-compatible chamber (Linkam Chamber) with electrical feedthrough. For temperature dependent measurements, a low-temperature controller was linked to the chamber and while using liquid nitrogen as the coolant. Time-resolved PL and EL (TRPL and TREL) measurements were conducted in a setup that incorporates with an avalanche photodetector and a time-correlated single-photon counting (TCSPC). For TREL measurement, the reference signal from function generator was synchronized to TCSPC as a start time tagger signal. The histogram measurement was performed by TCSPC, where the resolution of TCSPC could go down to 8 ps. It is noted that all EL spectra, TREL and EL mapping spectra were generated with 0.7V to 1V peak-to-peak voltage with frequency ranging from 100 kHz to 1.5 MHz. All spectra were corrected with the instrument response.

# Declarations

## Supplementary Information

All additional data and supplementary information and methods are presented in the Supplementary Information file available online. The figures and information in the Supplementary Information have been cited at appropriate places in this manuscript.

## Acknowledgements

We would like to acknowledge the financial support from ANU PhD student scholarship, China Scholarship Council, Australian Research Council, ANU Major Equipment Committee fund. We would also like to thank Professor Chennupati Jagadish's group from the Research school of Physics, the Australian National University for their facility support.

## Author Contributions

Y.L. conceived and supervised the project; Y.Z. and B.W prepared  $WS_2$  samples and LED device; Y. Z. designed experiments; Y.Z. and B.W carried out all the optical measurements; Y. Z. carried out the electrical measurements; Y. Z. and Y. L. analyzed the data; J.F. T. and W. L. contributed the experimental setup; Y. Z., B.W and Y. L. drafted the manuscript and all authors contributed to the manuscript.

## Competing financial interests

The authors declare that they have no competing financial interests.

# References

1. Gutiérrez HR, *et al.* Extraordinary room-temperature photoluminescence in triangular  $WS_2$  monolayers. *Nano Letters* **13**, 3447-3454 (2012).
2. Mak KF, Lee C, Hone J, Shan J, Heinz TF. Atomically thin  $MoS_2$ : a new direct-gap semiconductor. *Physical Review Letters* **105**, 136805 (2010).
3. Wang QH, Kalantar-Zadeh K, Kis A, Coleman JN, Strano MS. Electronics and optoelectronics of two-dimensional transition metal dichalcogenides. *Nature Nanotechnology* **7**, 699 (2012).
4. Liu Y, *et al.* Approaching the Schottky–Mott limit in van der Waals metal–semiconductor junctions. *Nature* **557**, 696-700 (2018).
5. Tang Y, *et al.* Tuning layer-hybridized moiré excitons by the quantum-confined Stark effect. *Nature Nanotechnology*, (2020).
6. Luo Y, *et al.* In situ nanoscale imaging of moiré superlattices in twisted van der Waals heterostructures. *Nature Communications* **11**, 4209 (2020).

7. Withers F, *et al.* Light-emitting diodes by band-structure engineering in van der Waals heterostructures. *Nature Materials* **14**, 301 (2015).
8. Ross JS, *et al.* Electrically tunable excitonic light-emitting diodes based on monolayer WSe<sub>2</sub> p-n junctions. *Nature Nanotechnology* **9**, 268 (2014).
9. Withers F, *et al.* WSe<sub>2</sub> light-emitting tunneling transistors with enhanced brightness at room temperature. *Nano Letters* **15**, 8223-8228 (2015).
10. Lien D-H, *et al.* Large-area and bright pulsed electroluminescence in monolayer semiconductors. *Nature Communications* **9**, 1229 (2018).
11. Han K, *et al.* Bright electroluminescence in ambient conditions from WSe<sub>2</sub> pn diodes using pulsed injection. *Applied Physics Letters* **115**, 011103 (2019).
12. Cho J, *et al.* Centimeter-Scale and Visible Wavelength Monolayer Light-Emitting Devices. *Advanced Functional Materials* **30**, 1907941 (2020).
13. Paur M, Molina-Mendoza AJ, Bratschitsch R, Watanabe K, Taniguchi T, Mueller T. Electroluminescence from multi-particle exciton complexes in transition metal dichalcogenide semiconductors. *Nature Communications* **10**, 1-7 (2019).
14. Chen J-h, Tan J, Wu G-x, Zhang X-j, Xu F, Lu Y-q. Tunable and enhanced light emission in hybrid WS<sub>2</sub>-optical-fiber-nanowire structures. *Light: Science & Applications* **8**, 1-8 (2019).
15. Hong YJ, *et al.* Visible-color-tunable light-emitting diodes. *Advanced Materials* **23**, 3284-3288 (2011).
16. Ubrig N, *et al.* Design of van der Waals interfaces for broad-spectrum optoelectronics. *Nature Materials* **19**, 299-304 (2020).
17. Zong X, *et al.* Black phosphorus-based van der Waals heterostructures for mid-infrared light-emission applications. *Light: Science & Applications* **9**, 114 (2020).
18. Ross JS, *et al.* Electrical control of neutral and charged excitons in a monolayer semiconductor. *Nature Communications* **4**, 1474 (2013).
19. Scholes GD, Rumbles G. Excitons in nanoscale systems. *Nature Materials* **5**, 683-696 (2006).
20. Palacios-Berraquero C, *et al.* Atomically thin quantum light-emitting diodes. *Nature Communications* **7**, 12978 (2016).
21. Zhang Y, *et al.* Probing Carrier Transport and Structure-Property Relationship of Highly Ordered Organic Semiconductors at the Two-Dimensional Limit. *Physical Review Letters* **116**, 016602 (2016).
22. Zhu Y, *et al.* High-Efficiency Monolayer Molybdenum Ditelluride Light-Emitting Diode and Photodetector. *ACS Applied Materials & Interfaces* **10**, 43291-43298 (2018).
23. Allain A, Kis A. Electron and hole mobilities in single-layer WSe<sub>2</sub>. *ACS Nano* **8**, 7180-7185 (2014).
24. Podzorov V, Gershenson M, Kloc C, Zeis R, Bucher E. High-mobility field-effect transistors based on transition metal dichalcogenides. *Applied Physics Letters* **84**, 3301-3303 (2004).
25. Guo Y, Liu D, Robertson J. Chalcogen vacancies in monolayer transition metal dichalcogenides and Fermi level pinning at contacts. *Applied Physics Letters* **106**, 173106 (2015).

26. Ovchinnikov D, Allain A, Huang Y-S, Dumcenco D, Kis A. Electrical transport properties of single-layer WS<sub>2</sub>. *ACS Nano* **8**, 8174-8181 (2014).
27. Sarkar S, Amin KR, Modak R, Singh A, Mukerjee S, Bid A. Role of different scattering mechanisms on the temperature dependence of transport in graphene. *Scientific Reports* **5**, 16772 (2015).
28. Carvalho A, Neto AC. Donor and acceptor levels in semiconducting transition-metal dichalcogenides. *Physical Review B* **89**, 081406 (2014).
29. Schuler B, *et al.* How Substitutional Point Defects in Two-Dimensional WS<sub>2</sub> Induce Charge Localization, Spin–Orbit Splitting, and Strain. *ACS Nano* **13**, 10520-10534 (2019).
30. Chow PK, *et al.* Defect-induced photoluminescence in monolayer semiconducting transition metal dichalcogenides. *ACS Nano* **9**, 1520-1527 (2015).

## Figures

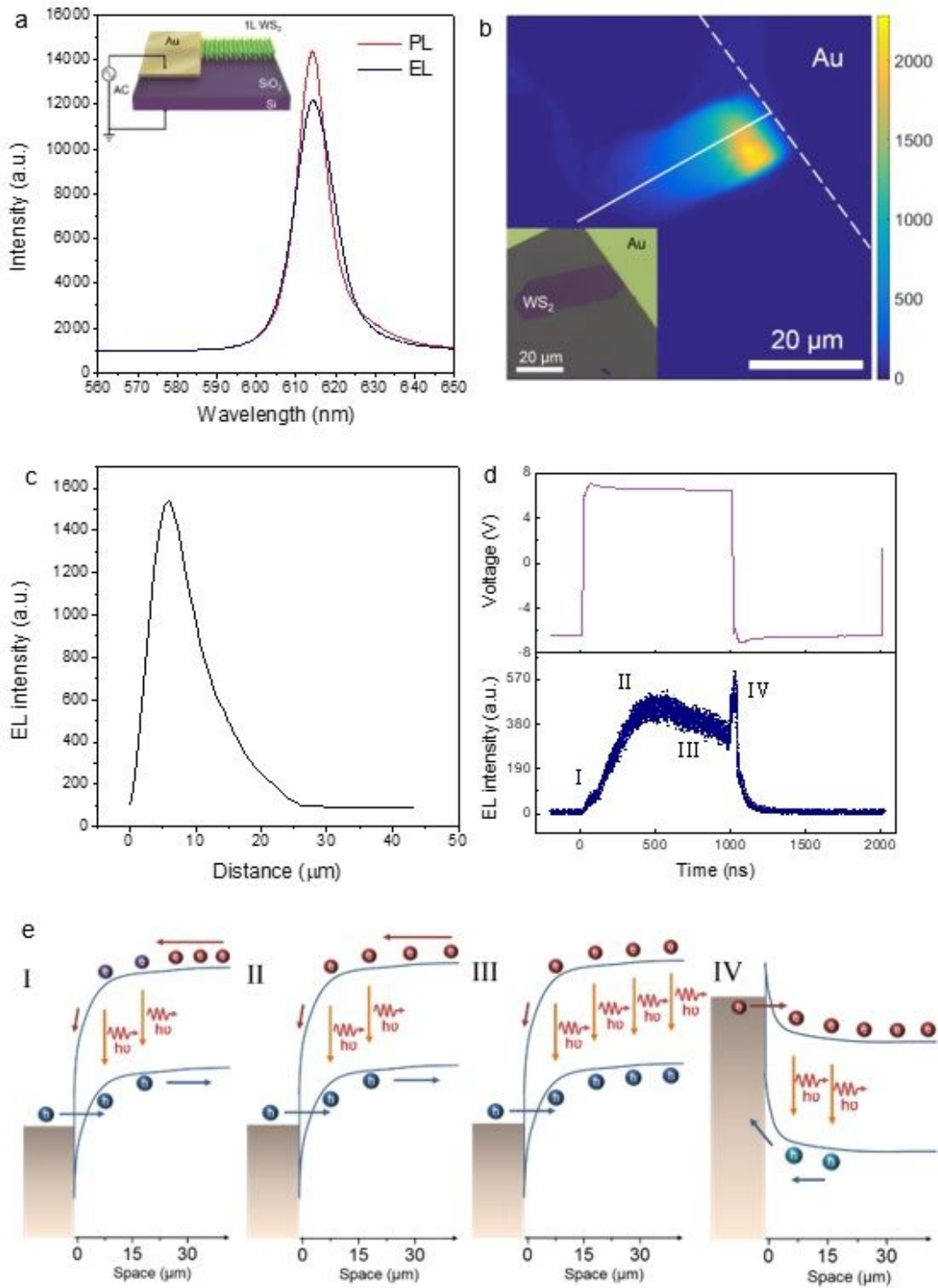


**Figure 1**

Monolayer WS<sub>2</sub> LED devices with large area and ultra-long EL emission length at room temperature and the principle of the continuous-pulsed emission mode. a EL and PL spectra measured for monolayer WS<sub>2</sub> devices ( $V_{ac} = 7.5$  V at 500 kHz). Inset: the schematic of AC LED devices. b EL mapping at 619 nm of the recorded WS<sub>2</sub> AC LED device with a large-area and the longest EL emission length ( $V_{ac} = 7.5$  V at 500k Hz). The white dashed line indicates the contacted edge of the gold electrode. Inset: the optical image of

this WS<sub>2</sub> device. c EL emission profile along the solid white line shown in b. d Time-resolved electroluminescence and their corresponding alternating driving voltage trace for WS<sub>2</sub> AC LED device. The driving voltages are  $\pm 6.6$  V and the driving frequency is 500 kHz. Two different decay behaviors indicate the unsymmetrical carrier recombination process at two voltage transients. e Schematic band diagrams corresponding to four emission phases labelled as I, II, III and IV in d.

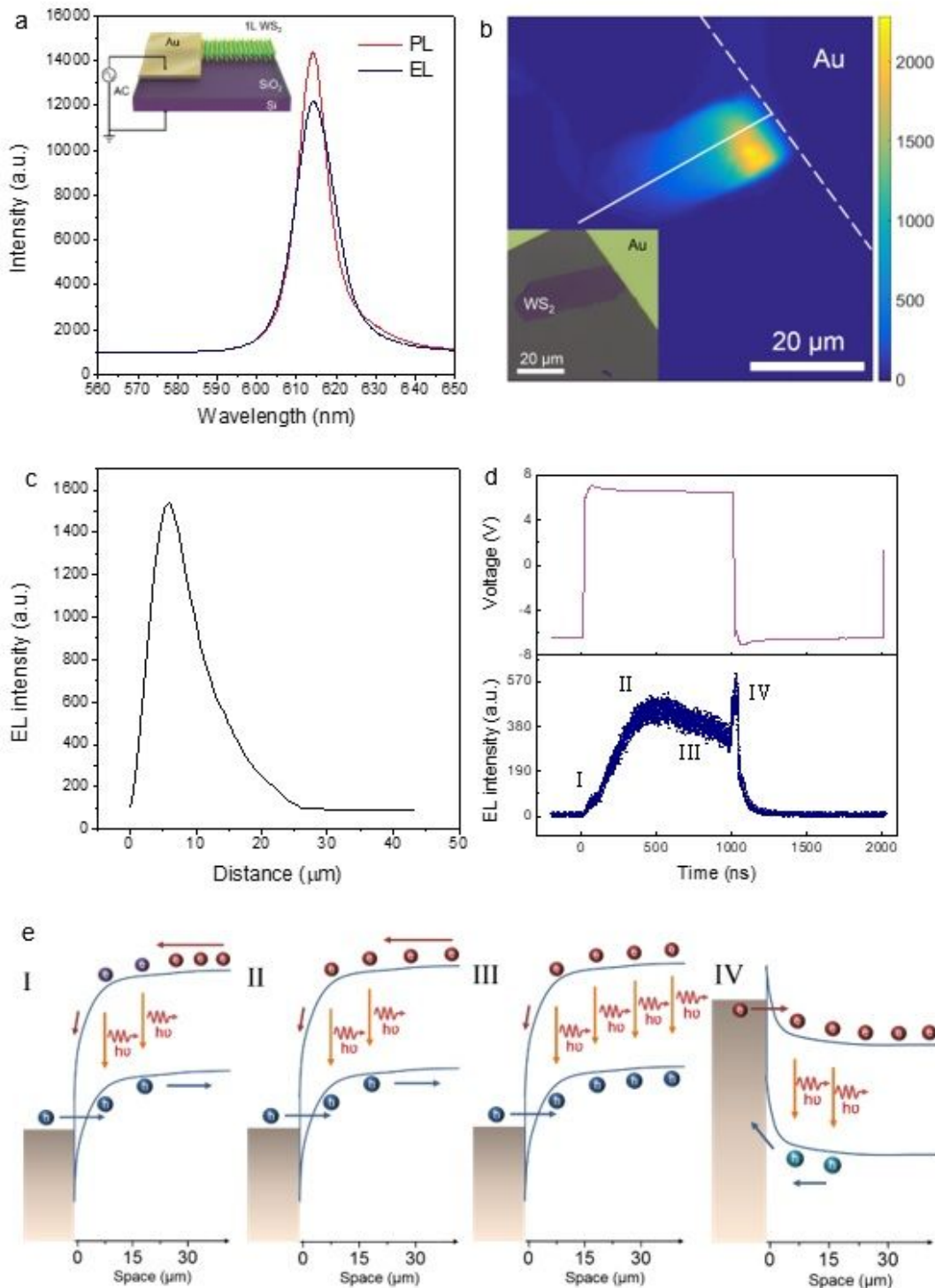


Figure 1

Monolayer WS<sub>2</sub> LED devices with large area and ultra-long EL emission length at room temperature and the principle of the continuous-pulsed emission mode. a EL and PL spectra measured for monolayer WS<sub>2</sub> devices (V<sub>ac</sub> = 7.5 V at 500 kHz). Inset: the schematic of AC LED devices. b EL mapping at 619 nm of the recoded WS<sub>2</sub> AC LED device with a large-area and the longest EL emission length (V<sub>ac</sub> = 7.5 V at 500 kHz). The white dashed line indicates the contacted edge of the gold electrode. Inset: the optical image of this WS<sub>2</sub> device. c EL emission profile along the solid white line shown in b. d Time-resolved electroluminescence and their corresponding alternating driving voltage trace for WS<sub>2</sub> AC LED device. The driving voltages are  $\pm 6.6$  V and the driving frequency is 500 kHz. Two different decay behaviors indicate the unsymmetrical carrier recombination process at two voltage transients. e Schematic band diagrams corresponding to four emission phases labelled as I, II, III and IV in d.

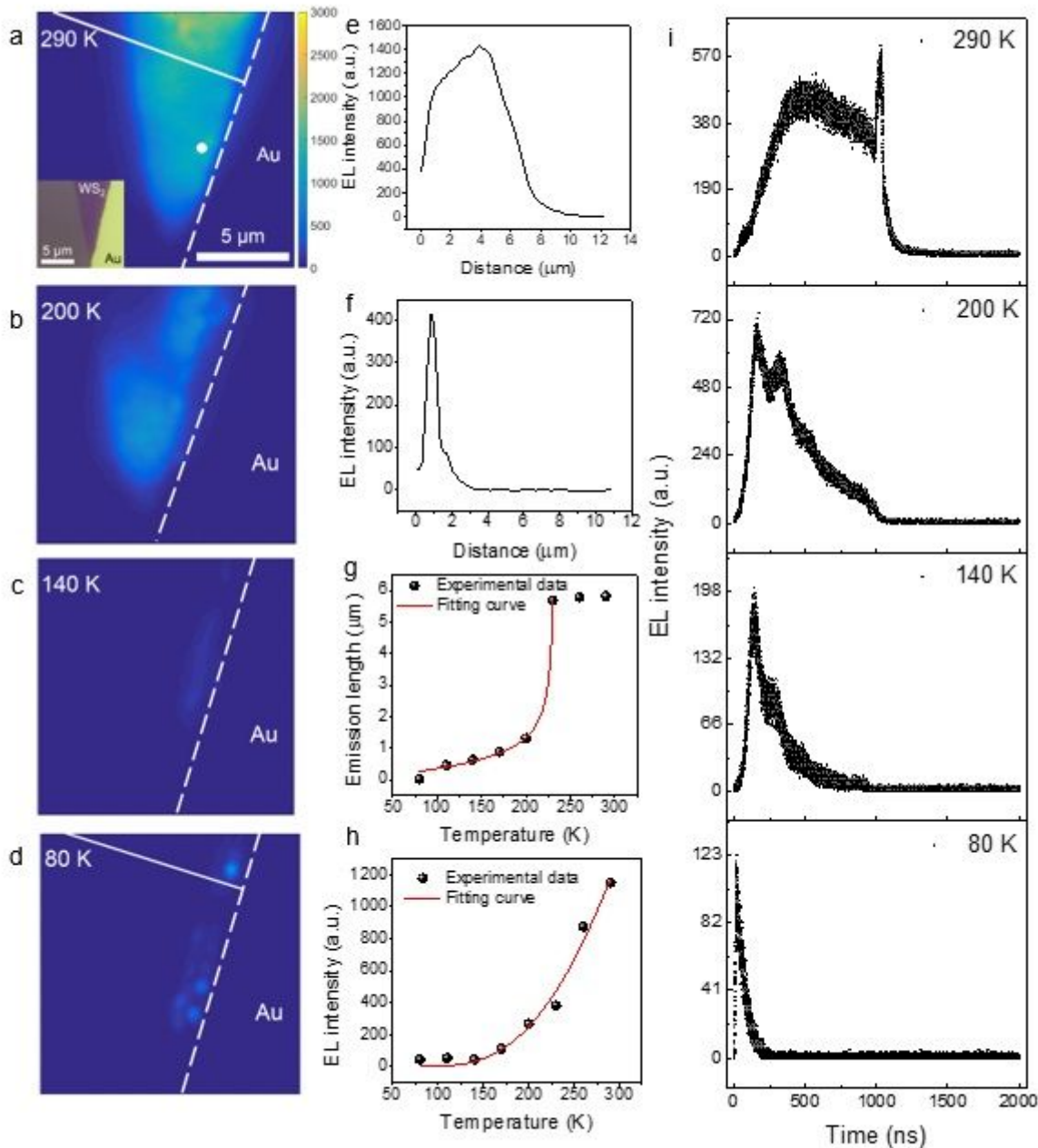
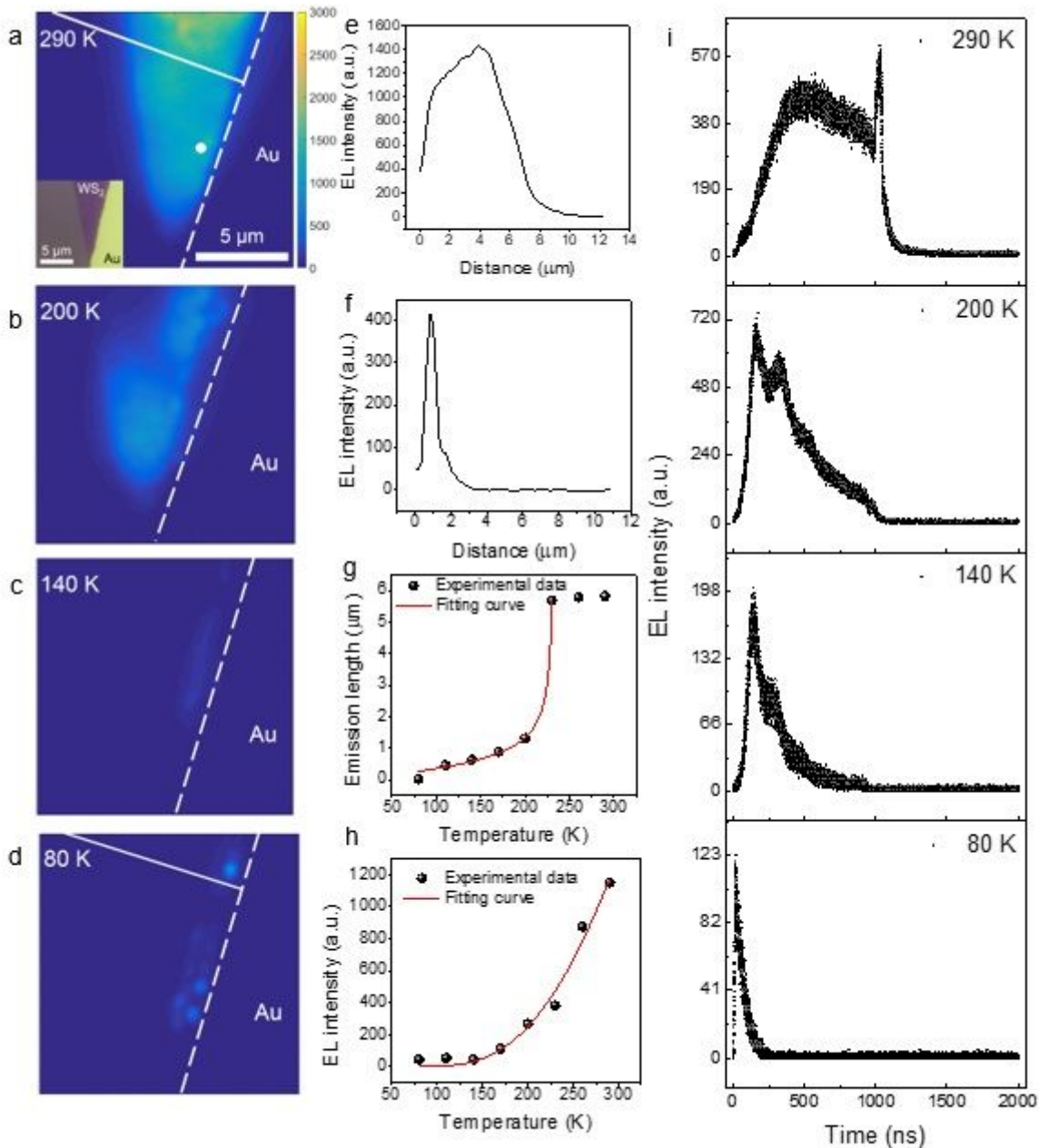


Figure 2

Temperature dependent EL emission length. a–d Temperature dependent EL emission mapping at 290 K, 200 K, 140 K and 80 K. Scale bar is 5  $\mu\text{m}$ . Inset: the optical image of this WS<sub>2</sub> device. e EL emission cross section profile along the solid white line in a. f EL emission cross section profile along the solid white line in d. g EL emission lengths as function of the temperature. The red solid line is fitting curve. h EL emission intensities as a function of temperature from the same single spot indicated as white dot in a. The red solid line is fitting curve. i, Temperature dependent time resolved electroluminescence at 290 K, 200 K, 140 K and 80 K.



**Figure 2**

Temperature dependent EL emission length. a–d Temperature dependent EL emission mapping at 290 K, 200 K, 140 K and 80 K. Scale bar is 5  $\mu\text{m}$ . Inset: the optical image of this WS<sub>2</sub> device. e EL emission cross

section profile along the solid white line in a. f EL emission cross section profile along the solid white line in d. g EL emission lengths as function of the temperature. The red solid line is fitting curve. h EL emission intensities as a function of temperature from the same single spot indicated as white dot in a. The red solid line is fitting curve. i, Temperature dependent time resolved electroluminescence at 290 K, 200 K, 140 K and 80 K.

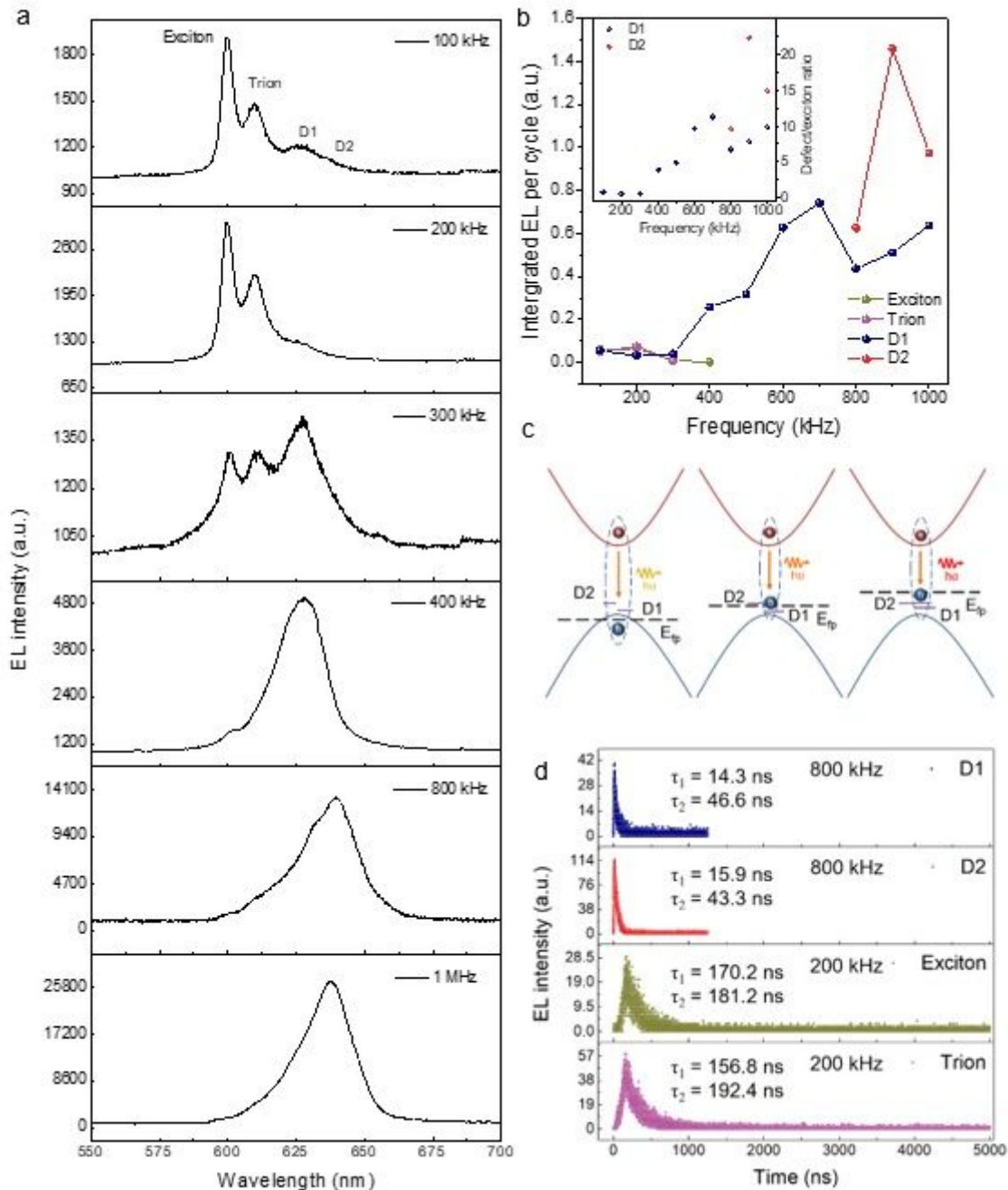


**Figure 3**

AC driving frequency induced wavelength tuneable EL emission. a Frequency dependent EL spectra from the monolayer WS<sub>2</sub> AC LED at 80k (V<sub>ac</sub> = 7.5 V). b Frequency normalized integrated intensities of four emission species versus AC driving frequency. Inset: defects and exciton emission ratio as function of AC

driving frequency. c Schematic band explanation of frequency induced exciton/trion to defect 1 (D1) and defect 2 (D2) transition. E<sub>fp</sub> represents the quasi Fermi level of holes. d Time resolved electroluminescence of exciton, trion, D1 and D2 species under driving frequency at 500 kHz.

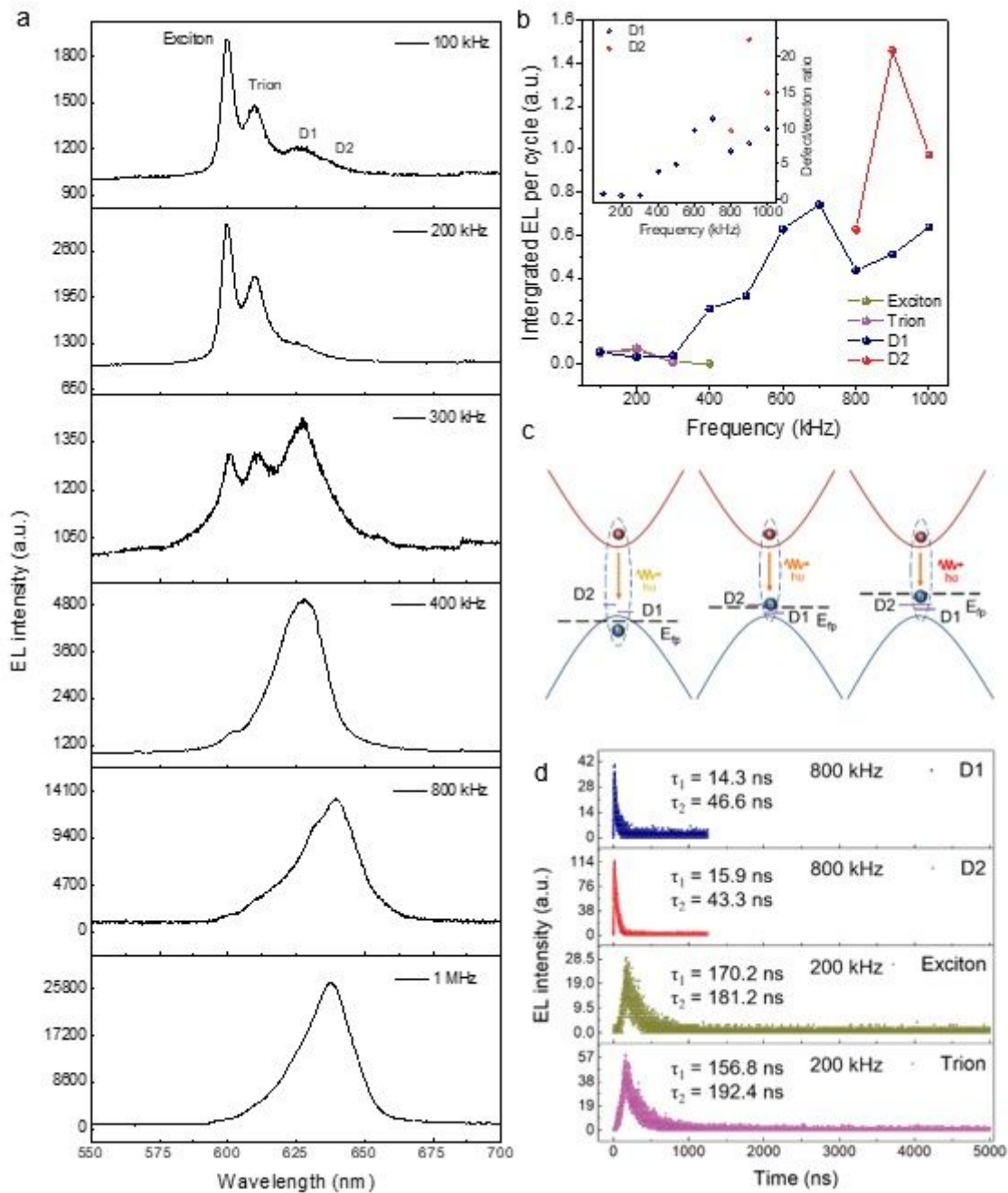


**Figure 3**

AC driving frequency induced wavelength tuneable EL emission. a Frequency dependent EL spectra from the monolayer WS<sub>2</sub> AC LED at 80k (V<sub>ac</sub> = 7.5 V). b Frequency normalized integrated intensities of four emission species versus AC driving frequency. Inset: defects and exciton emission ratio as function of AC driving frequency. c Schematic band explanation of frequency induced exciton/trion to defect 1 (D1) and

defect 2 (D2) transition. E<sub>fp</sub> represents the quasi Fermi level of holes. d Time resolved electroluminescence of exciton, trion, D1 and D2 species under driving frequency at 500 kHz.

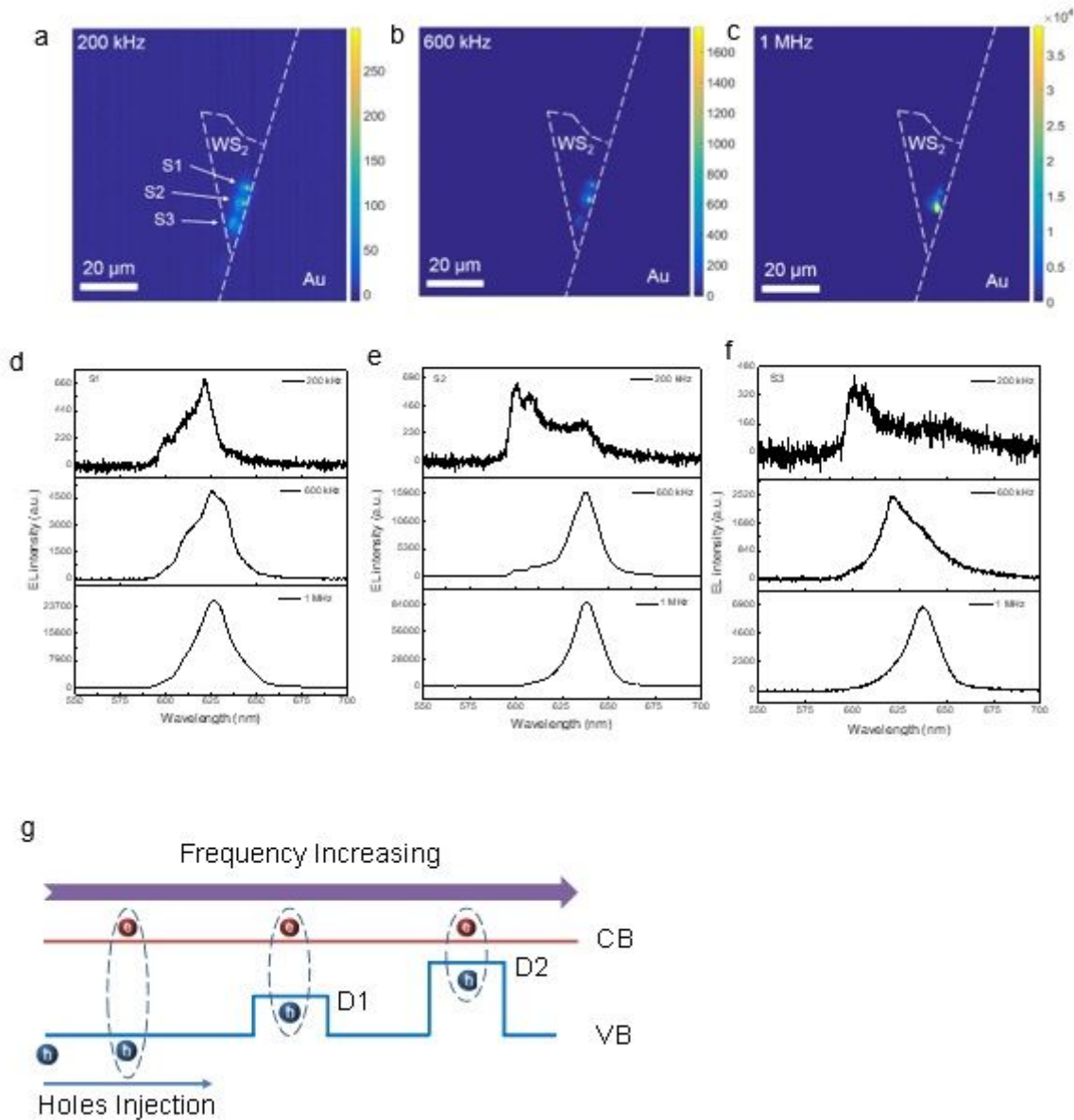


**Figure 4**

Visualization of exciton/trion to defect emission transition and defect levels evolution. a–c EL emission mapping of the same sample under driving frequency of 200 kHz, 600 kHz and 1 MHz, respectively. ( $V_{ac} = 7.5V$  at 80 K) d–f EL spectra of three different emission spots labelled as S1, S2 and S3 in a. For each panel, the driving frequency from top to bottom are 200 kHz, 600 kHz and 1 MHz. g Schematic of wavelength tunable EL emission with increasing AC frequency, where red and blue lines represent the conduction band and valence band, respectively.

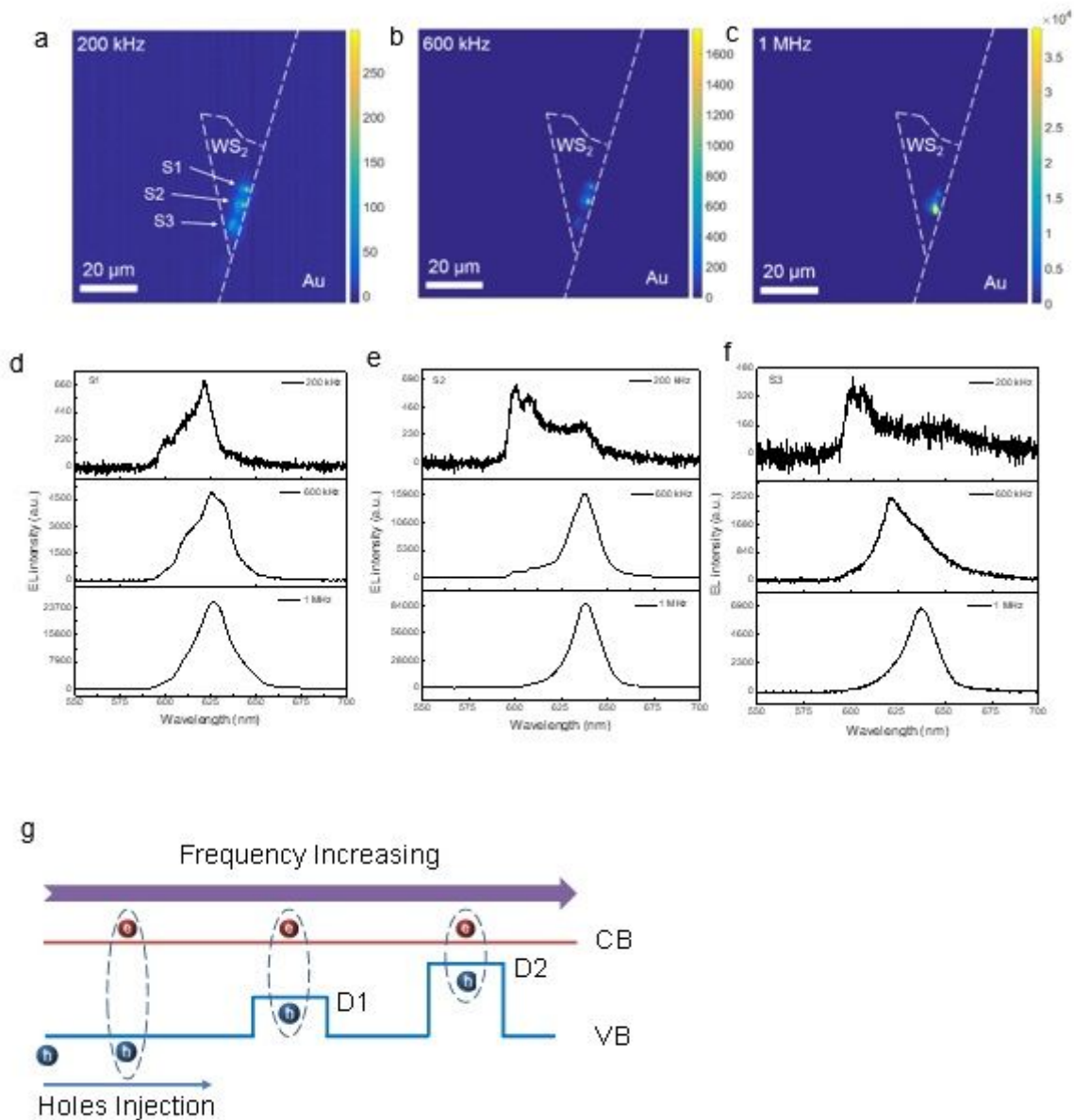


**Figure 4**

Visualization of exciton/trion to defect emission transition and defect levels evolution. a–c EL emission mapping of the same sample under driving frequency of 200 kHz, 600 kHz and 1 MHz, respectively. ( $V_{ac} = 7.5V$  at 80 K) d–f EL spectra of three different emission spots labelled as S1, S2 and S3 in a. For each panel, the driving frequency from top to bottom are 200 kHz, 600 kHz and 1 MHz. g Schematic of wavelength tunable EL emission with increasing AC frequency, where red and blue lines represent the conduction band and valence band, respectively.

## Supplementary Files

This is a list of supplementary files associated with this preprint. [Click to download.](#)

- [SupplementaryinformtionsubNC.docx](#)
- [SupplementaryinformtionsubNC.docx](#)